nature communications

Article

https://doi.org/10.1038/s41467-025-56471-z

Ocean wave-driven covalent organic framework/ZnO heterostructure composites for piezocatalytic uranium extraction from seawater

Received: 5 May 2024

Accepted: 15 January 2025

Published online: 27 January 2025

Check for updates

Jia-Xin Qi[1,2,3], Jing-Wen Gong[2,3], Cheng-Rong Zhang[1,3], Zhi-Hai Peng[2], Yuan-Jun Cai[2], Xin Liu[2], Jin-Lan Liu[2], Xiao-Juan Chen[2], Ru-Ping Liang[2] & Jian-Ding Qiu[1,2]

Piezoelectric catalysis possesses the potential to convert ocean wave energy into and holds broad prospects for extracting uranium from seawater. Herein, the Z-type ZnO@COF heterostructure composite with excellent piezoelectric properties was synthesized through in situ growth of covalent organic frameworks (COFs) on the surface of ZnO and used for efficient uranium extraction. The designed COFs shell enables ZnO with stability, abundant active sites and high-speed electron transport channels. Meanwhile, the interface electric field established in the heterojunctions stimulates electron transfer from COFs to ZnO, which break the edge shielding effect of the ZnO's metallic state. Additionally, the polarization of ZnO is enhanced by heterogeneous engineering, which ensures the excellent piezocatalytic performance. As a result, ZnO@COF achieves an ultra-high efficiency of 7.56 mg g^{-1} d^{-1} for uranium extraction from natural seawater driven by waves. In this work, we open an avenue for developing efficient catalysts for uranium extraction from seawater.

Efficient and economical uranium extraction from seawater is expected to ensure the long-term sustainability of nuclear power[1,2]. Covalent organic frameworks (COFs) are advanced porous materials that precisely integrate multiple functional units, making them ideal for efficiently extracting uranium from seawater[3–5]. At present, a number of COF-based seawater uranium extraction techniques have been developed[6–8]. However, the traditional adsorption method shows inefficient adsorption because the concentration of seawater uranium is very low at 3.3 ppb[9–11]. Harnessing solar energy to convert soluble uranium into insoluble forms is a promising approach to improve the efficiency of seawater uranium capture[12–14]. Regrettably, photocatalytic methods are limited by time (day or night), geography, and seasons, and require sacrificial agents for effective charge separation, limiting their practical application[13,15]. The emergence of electrocatalytic technology realizes the continuous uranium extraction from seawater and greatly improves the extraction efficiency[16,17]. However, this approach requires an additional electric field, contradicting the goals of green and sustainable development strategies[18]. Therefore, it is crucial to advocate sustainable development and explore innovative energy sources for uranium extraction from seawater. However, the ocean's vast and stable wave energy remains untapped for this purpose, which will raise both hopes and challenges for the sustainable seawater uranium extraction[19,20].

[1]National Key Laboratory of Uranium Resource Exploration-Mining and Nuclear Remote Sensing, East China University of Technology, Nanchang 330013, China. [2]School of Chemistry and Chemical Engineering, Nanchang University, Nanchang 330031, China. [3]These authors contributed equally: Jia-Xin Qi, Jing-Wen Gong, Cheng-Rong Zhang. e-mail: jdqiu@ncu.edu.cn

Piezoelectric catalysis serves as the bridge for converting mechanical energy into chemical energy[21–23]. It can be stimulated by external mechanical vibrations to induce polarization, and generate piezoelectric potential to form an internal electric field, thereby promoting the production of active free radicals[24–26]. Moreover, piezoelectric catalysis can also enhance charge separation, thus minimizing dependence on sacrificial agents[27–29]. Therefore, it seems that piezocatalysis has the potential to efficiently enrich seawater uranium using wave energy. Regrettably, COFs have good performance but fall short in displaying innate piezoelectric effects, making them less than ideal for piezoelectric uranium extraction alone. Hence it is necessary to utilize materials with piezoelectric properties to endow COFs this capability. This collaborative partnership will unleash the combined potential of COFs and piezoelectric materials, which expand the applications of COFs and highlight their importance in environmentally friendly catalysis and resource extraction.

Among the reported piezoelectric materials, ZnO is considered as an ideal piezoelectric catalysis due to its excellent properties derived from the non-centrosymmetric fibrillar zincite structure[30–32]. However, single ZnO has a wide bandgap and encounters significant electron transfer resistance[33,34]. Therefore, the piezoelectric efficiency and practicality of ZnO can be improved by using inorganic materials with aligned band positions to fabricate heterojunctions, such as CuI/ZnO[35], FTC-ZnO[36] and GQDs/ZnO[37]. However, these materials have very poor tunability, so their heterogeneous engineering with ZnO are usually limited to local interface control, often ignoring the metal edge shielding effect and material instability problems of ZnO[38,39]. In sharp contrast, the strategic deployment of highly adaptable COFs in ZnO heterogeneous engineering promises to precisely address obstacles[40–42]. Unfortunately, the visionary concept of building heterostructures through covalent bond connections between ZnO and COFs remains an uncharted territory, with the potential in piezoelectric catalysis waiting to be awakened.

In this work, covalently bonded ZnO@COF core-shell hybrid materials were innovatively synthesized by in-situ growth of COFs on the aminated surface of ZnO. The ZnO as the core endows piezoelectric performance to the heterojunctions, while the outer COFs shell layer provides high-speed highway for electron transport and abundant catalytic active sites, and enhances the stability of the heterojunctions. Simultaneously, the interfacial electric field established inside the heterojunctions extends across the entire surface of ZnO edges, effectively destroying the metal edge shielding effect and accelerating the electron-hole separation. Benefiting from the collaboration between ZnO and COF improves the polarization of the heterojunctions, making its piezoelectric performance efficiency far superior to those traditional piezoelectric materials. As expected, ZnO@COF exhibited excellent piezocatalytic efficiency and achieves efficient extraction of uranium from seawater. This study provides an effective strategy for uranium extraction using wave energy.

Results

Heterojunction of ZnO@COF

A schematic illustration of the ZnO@COF Z-type heterojunction is shown in Fig. 1a. ZnO nanospheres were prepared by solvothermal using $Zn(OAc)_2 \cdot 2H_2O$ as precursor[38]. Then ZnO nanospheres were modified with 3-aminopropyltriethoxysilane (APTES) to obtain amino-functionalized ZnO nanospheres (ZnO-APTES). Subsequently, ZnO@COF core-shell hybrid materials with different COF ratios were constructed by growing COF (TP-BDOH, where TP denotes 2,4,6-triformylphloroglucinol and BDOH refers to 3,3′-dihydroxybenzidine) on ZnO-APTES in situ via a Schiff base reaction. The morphologies of ZnO nanospheres, COF, and ZnO@COF were characterized using scanning electron microscopy (SEM). The synthesized ZnO nanospheres show a well-defined spherical morphology with an average diameter of 150 ± 20 nm (Supplementary Fig. 1a). The prepared COF exhibits a fibrous network structure assembled by nanowires (Supplementary Fig. 1b). From the SEM images of ZnO@COF (Supplementary Fig. 1c–f), it is clear that ZnO nanospheres are uniformly wrapped by the fibrous COF. Comparing transmission electron microscopy (TEM) of ZnO and ZnO@COF (Fig. 1b, c), it also confirms that ZnO nanoparticles are completely coated with the COF layer with a thickness of about 20 nm, indicating a strong bonding interaction between ZnO and COF[24]. Furthermore, the high-resolution TEM (HR-TEM) images of ZnO@COF shoe that two distinct crystal planes are in close contact (Fig. 1d). The lattice spacings are 0.28 nm and 0.26 nm, which correspond to the (1 0 0) planes of ZnO and COF respectively, confirming the successful synthesis of the heterostructure. Elemental mapping images (EDS) shows that C, N, O, and Zn are densely distributed of on the surface of ZnO@COF, which further proves the uniform encapsulation of ZnO by COF (Supplementary Fig. 2). The thermal stability of the synthesized ZnO, COF, and ZnO@COF was analyzed using thermo gravimetric analysis (TGA), revealing excellent thermal stability below 320 °C under N_2 atmosphere (Supplementary Fig. 3).

In order to accurately evaluate the properties of the materials, a series of heterojunctions named ZnO@COF-x were synthesized by adjusting the ratio of COF (x represents the percentage of COF). The crystal structure and crystallinity of the synthesized samples were analyzed using powder X-ray diffraction (PXRD). The main diffraction peak of COF at 3.45° corresponds to the (1 0 0) crystal plane (Supplementary Fig. 4), which is consistent with the simulated results and confirms the formation of a long-range ordered crystal structure[43]. ZnO nanospheres have hexagonal wurtzite phase (PDF 89-1397), and the main diffraction peaks are located at 31.74°, 34.38°, and 36.21° of the (1 0 0), (0 0 2), and (1 0 1) crystal planes, respectively (Supplementary Fig. 5). A series of distinct characteristic diffraction peaks corresponding to ZnO and COF can be observed in the XRD patterns of ZnO@COF, which indicate the successful synthesis of the heterojunctions (Fig. 2a). Furthermore, the coexistence of ZnO and COF in the Fourier-transform infrared (FT-IR) spectra of ZnO@COF further proves that COF is successfully grafted to the ZnO surface by Schiff base reaction (Supplementary Figs. 6 and 7).

To explore the surface composition and chemical interactions in the ZnO@COF heterojunctions, X-ray photoelectron spectroscopy (XPS) characterization was conducted. The XPS measurements confirms the presence of C, N, O, and Zn elements within the ZnO@COF heterojunctions, further substantiating the successful synthesis of the composites (Fig. 2b). Notably, a shift towards lower binding energy for the Zn 2*p* core level is observed in the ZnO@COF heterojunction compared to pure ZnO (Fig. 2c). This shift indicates an increase in the electron cloud density around ZnO, suggesting enhanced electronic interactions within the heterojunction[44]. On the contrary, the C 1*s* and N 1*s* peaks in ZnO@COF are shifted to higher energy levels compared to that of pure COF (Fig. 2d, e), demonstrating a decrease in the electron cloud density around COF, further highlighting the significant changes in the internal electronic environment of the heterojunctions[45].

The O 1*s* spectra are divided into two main peaks: C = O/C-O-H and Zn-O (Fig. 2f). The peaks of C = O/C-O-H and Zn-O are shifted to higher energy levels and lower energy levels respectively, which are consistent with the above results and become more obvious with the increase of COF content. These detailed spectral changes not only reveal the strong interaction between ZnO and COF, but also indicate the directionally induced migration of electrons from COF to ZnO due to close contact at the interface, thereby forming an effective internal electric field in the heterojunction[21]. The formed internal electric field is essential for promoting charge carrier separation and migration in the

https://doi.org/10.1038/s41467-025-56471-z

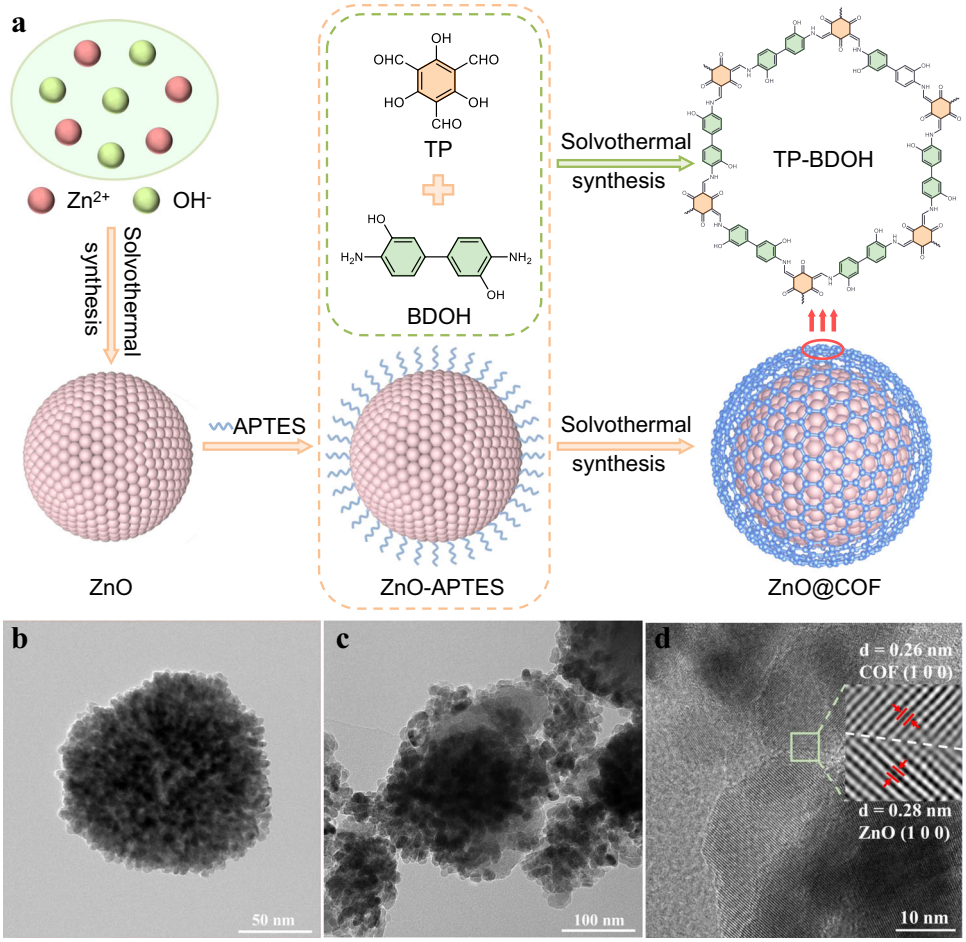

Fig. 1 | Synthesis and morphology of ZnO@COF. a Synthesis of ZnO, COF, and ZnO@COF (TP: 2,4,6-triformylphloroglucinol; BDOH: 3,3′-dihydroxybenzidine; APTES: 3-aminopropyltriethoxysilane). TEM images of **b** ZnO and **c** ZnO@COF. **d** HR-TEM image of ZnO@COF.

ZnO@COF heterojunction, and its effectiveness significantly enhanced with increasing COF content.

Piezoelectric properties of ZnO@COF

The piezoelectric effect is induced by the mechanical force acting on piezoelectric crystals, resulting in the formation of internal electric fields that drives various catalytic reactions. The corresponding morphology of the samples was characterized by atomic force microscopy (AFM). The AFM images of ZnO and ZnO@COF show that they have similar morphologies (Fig. 3a, b), and the particles of ZnO@COF are slightly thicker than that of ZnO by about 20 nm. The local piezoelectric response of samples was analyzed by Kelvin probe force microscopy (KPFM). Figure 3c, d show the surface potential images of ZnO and ZnO@COF in a 5 × 5 μm^2 field of view, illustrating their piezoelectric response properties. Under stress at the probe tip, ZnO@COF forms an internal electric field and generates a positive surface voltage of up to 71.57 mV, which is significantly higher than that of ZnO (1.71 mV) (Fig. 3e, f). Piezoforce response microscopy (PFM) was employed to quantify the piezoelectric response of the materials. The corresponding amplitudes and phase images of ZnO and ZnO@COF in the visual field of 5 × 5 μm^2 are presented in Supplementary Figs. 8 and 9, respectively. As displayed in Fig. 3g and h, the piezoelectric hysteresis curves of ZnO and ZnO@COF show a typical butterfly shape under ± 10 V DC bias electric field, and the phase angle is revered by 180°. The piezoelectric constant (d_{33}) values of ZnO and ZnO@COF are 10.4 pm V^{-1} and 48.1 pm V^{-1}, respectively, confirming the enhanced piezoelectric property exhibited by ZnO@COF. This discovery is attributed to the enhanced polarization of the heterojunction structure ZnO@COF, increasing the piezoelectric potential response at the interface. The further increase in piezoelectric current density in ZnO@COF compared to ZnO and COF (Fig. 3i) also provides additional evidence for stronger piezoelectric properties after the formation of the heterojunction between ZnO and COF. It is noteworthy that with the increase of COF content in heterojunction, the piezoelectric performance also improves correspondingly. This phenomenon can be attributed to that, with the increase of COF content, the direct interaction force between ZnO and COF is strengthened, and the efficiency of electron transfer is enhanced. However, excess COF content can provide place for electrons and holes to recombine, leading to a decline in piezoelectric performance of the heterojunction[24].

To gain insights into the underlying mechanisms inherent in the enhanced piezoelectric performance of heterojunction, the electronic property of ZnO, COF, and ZnO@COF heterojunction was studied. Electrochemical impedance spectroscopy (EIS) results show that ZnO@COF-40 has a smaller semicircular Nyquist plot radius than those of ZnO and COF (Fig. 4a), indicating lower electron transfer resistance. This evidence underscores that the incorporation of COFs with π-conjugated frameworks within ZnO established an internal electric field at the interface, resulting in significant polarization charges along the edges of ZnO. This reduces the shielding effect of ZnO's metal-edge states, promoting efficient charge transfer and enhancing electrical conductivity. In steady-state photoluminescence (PL) spectra, the PL peaks of ZnO, COF, and ZnO@COF are centered at 480 nm (Fig. 4b). While the peak intensity of ZnO@COF-40 is significantly reduced, indicating the suppression of

https://doi.org/10.1038/s41467-025-56471-z

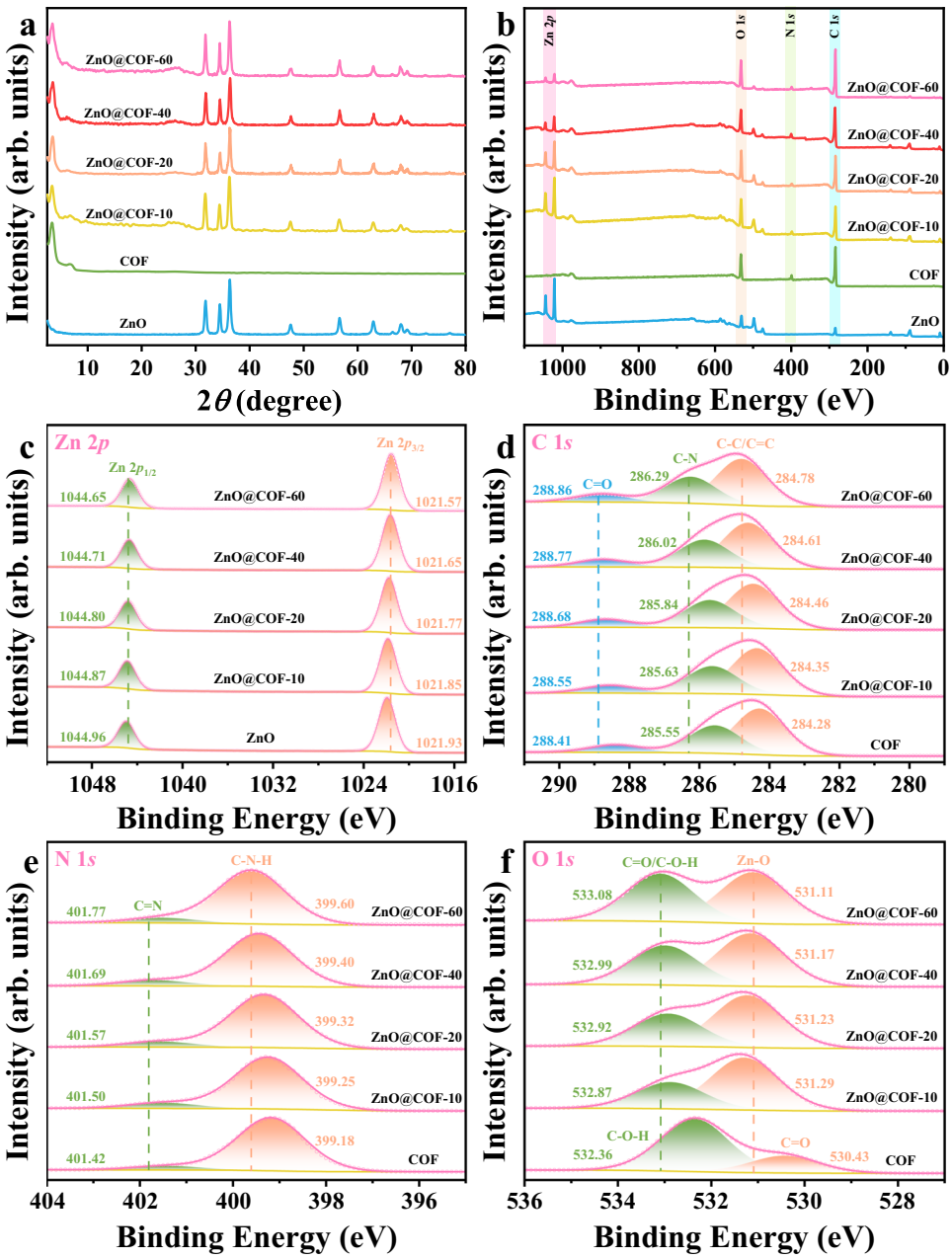

Fig. 2 | Composition and chemical interactions of ZnO@COF. a PXRD patterns, **b** XPS spectra survey, **c** Zn 2*p*, **d** C 1*s*, **e** N 1*s*, **f** O 1*s* of ZnO, COF, and ZnO@COF (c-f are XPS results of regions from the survey in b). The patterns of Fig. 2 are stacked. Source data for Fig. 2 are provided as a Source Data file.

carrier recombination in ZnO@COF-40. At the same time, time-resolved photoluminescence (TRPL) spectra were employed to characterize the lifetimes of samples. As shown in Fig. 4c, the fluorescence lifetimes of ZnO@COF composites are longer than those of ZnO and COF, and increase with the content of COF until it slightly decreased when the percentage content is 60. This can be attributed to the increased COF content facilitating carrier transport, thereby inhibiting the recombination of holes and electrons. However, when COF content becomes excessive, some electrons and holes may recombine on COF surface, leading to a decline in piezoelectric performance.

The optical absorption capabilities and electronic band structures of the samples were investigated by diffuse reflectance spectroscopy (DRS) and Mott-Schottky (M-S) spectroscopy. As shown in Supplementary Fig. 10, all the samples exhibit strong visible light absorption. Based on Kubelka-Munk calculations, the bandgaps for ZnO, COF, ZnO@COF-10, ZnO@COF-20, ZnO@COF-40, and ZnO@COF-60 are determined to be 3.18 eV, 1.91 eV, 1.88 eV, 1.83 eV, 1.79 eV, and 1.64 eV, respectively. It is observed that the bandgap of the composite materials gradually decreases with increasing COF content. Combined with the Mott-Schottky test results, it is clear that the band structure of catalysts fully corresponds to the equilibrium potential required for uranium reduction (Supplementary Fig. 11). Notably, the conduction band position of ZnO@COF-60 is close to the equilibrium potential for uranium reduction (Fig. 4d). However, piezoelectric materials effectively modulate the potential barrier of the material's electron band, which may cause ZnO@COF-60 to fail to meet the equilibrium potential of uranium reduction, thus weakening its catalytic effect.

As expected, the introduction of porous COF increases the specific surface area and pore volume of the heterojunction, which facilitates the adsorption of target and provides more active sites for piezoelectric catalytic reaction. The surface area and porosity of COF

https://doi.org/10.1038/s41467-025-56471-z

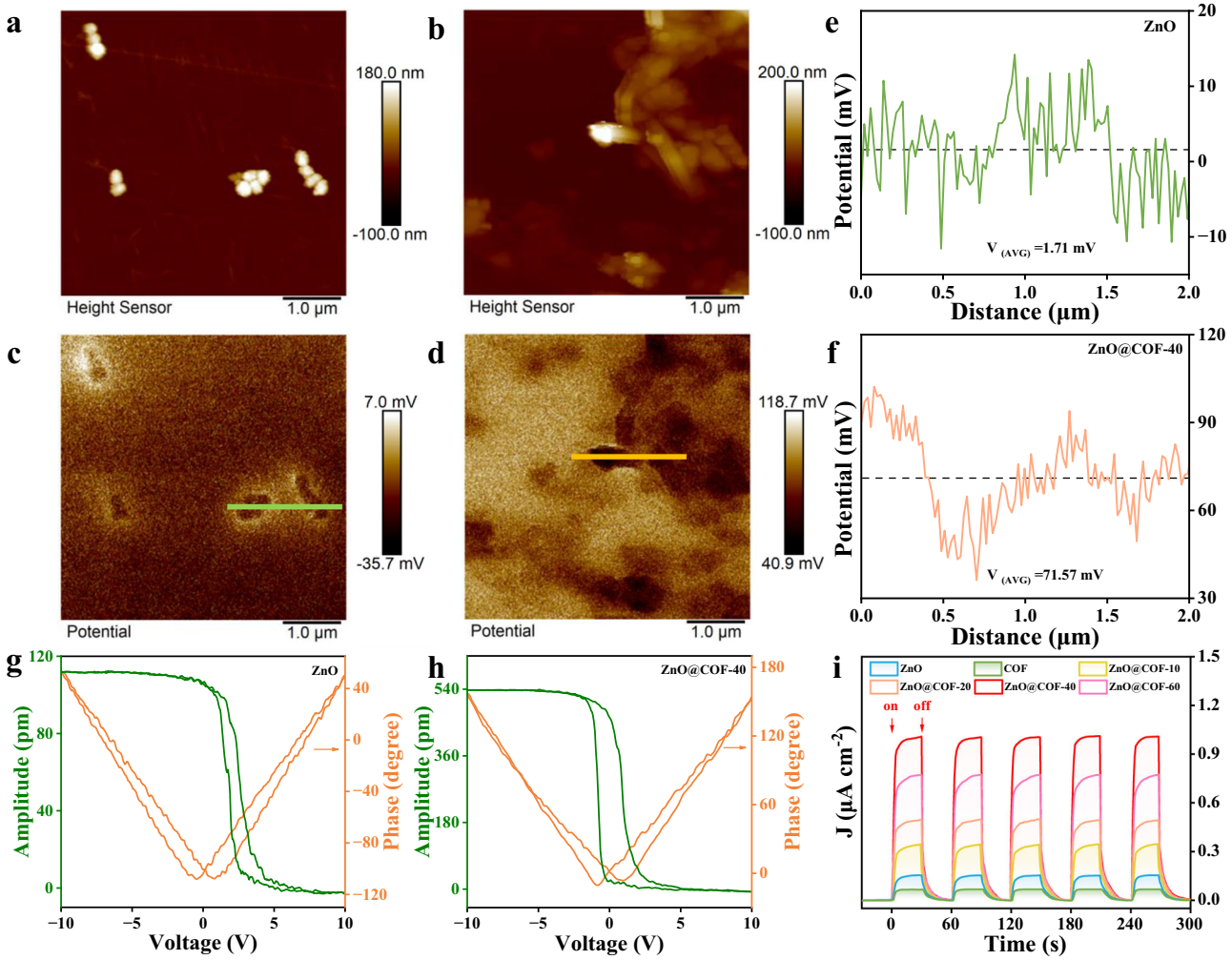

Fig. 3 | Piezoelectric property of ZnO and ZnO@COF. The topographic AFM (atomic force microscopy) images of **a** ZnO and **b** ZnO@COF. The surface KPFM (kelvin probe force microscopy) potential images of **c** ZnO and **d** ZnO@COF. Surface piezoelectric potentials of **e** ZnO and **f** ZnO@COF (e and f are the linescans from c and d). Piezoresponsive amplitude curve and phase curve of **g** ZnO and **h** ZnO@COF. **i** Transient piezoelectric current response of ZnO, COF, and ZnO@COF. Source data for Fig. 3 are provided as a Source Data file.

and the best performing ZnO@COF-40 were investigated through nitrogen adsorption-desorption isotherms based on the Brunauer-Emmett-Teller (BET) theory. Both COF and ZnO@COF-40 exhibit similar adsorption isotherms, which are classical type I isotherms, indicating their microporous characteristics (Supplementary Fig. 12). The specific surface area of ZnO@COF-40 is 319.22 $m^2 g^{-1}$, which is slightly lower than that of COF (377.73 $m^2 g^{-1}$), but still retains the inherent characteristics of COF. According to non-local density functional theory (NLDFT), the pore size distribution of COF and ZnO@COF-40 are concentrated around 1.41 nm (Supplementary Fig. 13). Therefore, the composite of ZnO@COF-40 demonstrates exceptional piezoelectric catalytic properties while retaining a high specific surface area, indicating its great potential as an excellent catalyst.

Piezocatalytic extraction of uranium

The ability of ZnO@COF-40 to remove 100 ppm U(VI) by piezoelectric catalysis was evaluated by ultrasonic treatment at 40 kHz and 120 W without the need for any organic sacrificial agents. As shown in Fig. 5a and Supplementary Fig. 14, due to the shielding effect of metallic edge states, the effective piezoelectric catalytic removal rate of ZnO is only 11.57%. COF exhibits a minimal piezoelectric uranium reduction rate of 19.72%, which is attributed to the rapid recombination of electron-hole pairs. In contrast, the physical mixing of ZnO and COF still shows a weaker uranium removal efficiency of 16.73%, but the piezoelectric catalytic activity of composite samples is significantly enhanced. Among them, ZnO@COF-40 exhibits the fastest adsorption kinetics, removing 95.25% of 100 ppm U within 1 min, following a pseudo-second-order model (Supplementary Fig. 15 and Supplementary Table 1). This phenomenon can be attributed to the formation of an internal electric field between ZnO and COF, which helps to successfully overcome the shielding effect of ZnO metal edge states. The generated piezoelectric internal electric field can effectively modulate charge carrier transport and suppress the rapid recombination of electron-hole pairs. Considering the variations of water environments under different conditions, the uranium capture capacity of piezoelectric catalysis was studied under the condition of 100 ppm uranium at pH 2-8 (Supplementary Fig. 16). Excitingly, ZnO@COF-40 exhibits higher removal performance under acidic conditions than those of ZnO and COF, maintaining excellent uranium removal efficiency over a wider pH range. This difference may be due to the limited carrier recombination at the interface between ZnO and COF after combination, which is conducive to the enhancement of piezoelectric catalytic activity. Subsequently, adsorption kinetics experiments of ZnO@COF-40 were carried out to verify the effectiveness of the piezoelectric material in capturing uranium (Fig. 5b and Supplementary Table 2). Encouragingly, the adsorption capacity of ZnO@COF-40 under

https://doi.org/10.1038/s41467-025-56471-z

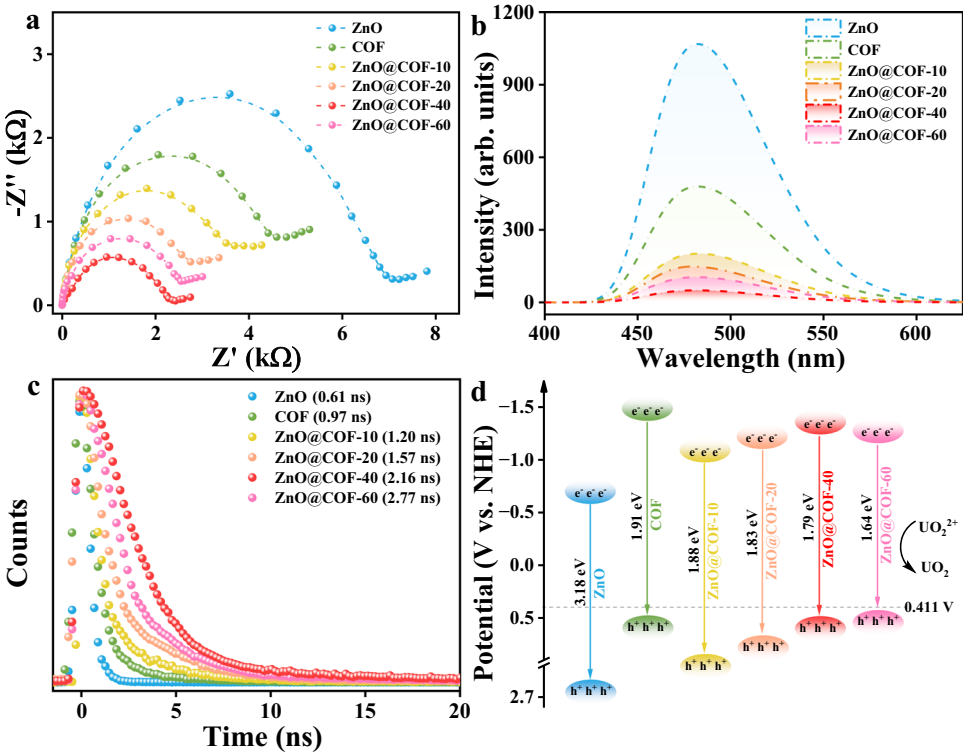

Fig. 4 | Electronic property of ZnO, COF and ZnO@COF. a Nyquist plots, **b** PL spectra, **c** TRPL spectra, **d** Band-structure diagram of ZnO, COF, and ZnO@COF. Source data for Fig. 4 are provided as a Source Data file.

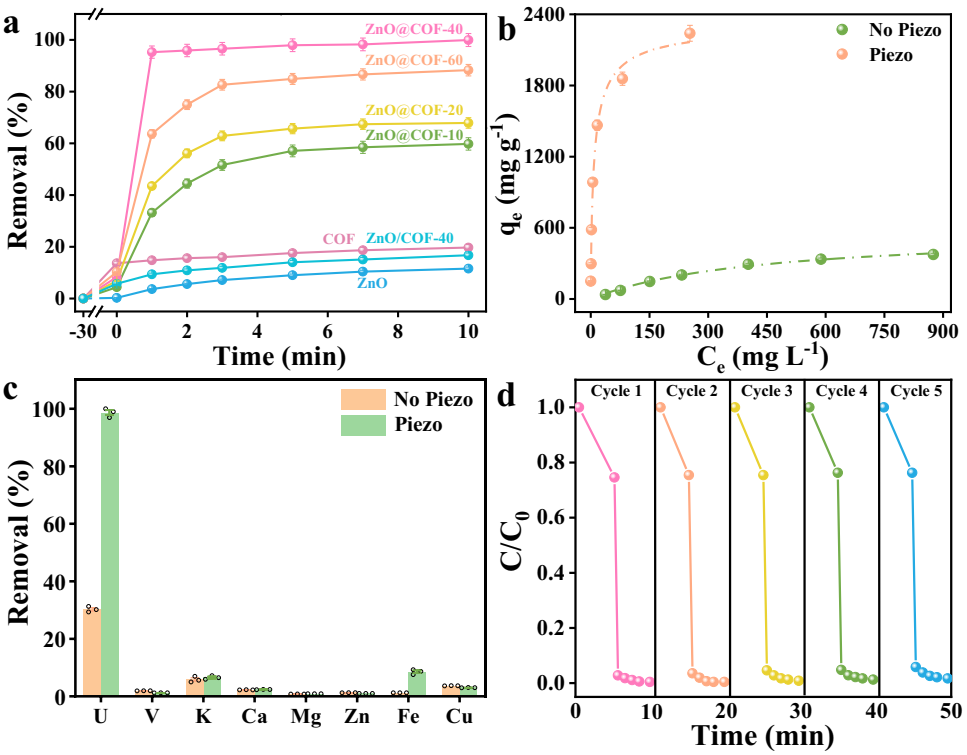

Fig. 5 | Performance of ZnO@COF piezoelectric catalyzed uranium extraction. a The piezo catalytic performance of U(VI) by ZnO, COF, and ZnO@COF after 10 min of ultrasonic ($C_{U(VI)}$ = 100 mg L^{-1}, pH 5). **b** The adsorption isotherm of UO_2^{2+} on ZnO@COF-40 under ultrasonic and without ultrasonic (pH 5). **c** The uranium removal rate of ZnO@COF-40 in the presence of competitive cations containing 10 ppm U. **d** Recyclability study of ZnO@COF-40 for U(VI) extraction. Error bars represent S.D. $n = 3$ independent experiments. Source data for Fig. 5 are provided as a Source Data file.

ultrasonic treatment is up to 2336.74 mg g^{-1}, far exceeding the adsorption capacity without ultrasonic treatment (389.67 mg g^{-1}). Under ultrasonic irradiation, a large amount of piezoelectric charge is generated in ZnO@COF-40. This leads to the reduction of U(VI) adsorbed on the ZnO@COF-40 surface to insoluble U(IV), which is beneficial to improve the utilization of active sites and obtain higher uranium adsorption capacity.

It is well known that many cations and anions coexist with U(VI) in seawater, and the presence of these ions greatly affects the adsorption and migration of the target metal ions. Therefore, the selectivity of ZnO@COF-40 for U(VI) by piezoelectric catalysis was investigated. As shown in Fig. 5c and Supplementary Fig. 17, ZnO@COF-40 selectively extracts U(VI) with little effect from other competing ions. The excellent selectivity of ZnO-COF-40 for U(VI) is due to its abundance of hydroxyl and aldehyde groups capable of forming stable chelates with uranium ions. High extraction performance and good selectivity help ZnO@COF-40 to effectively extract uranium in complex water environments, which is of great practical importance. Furthermore, through five consecutive cycles of experiments, ZnO@COF-40 continues to show high piezoelectric catalytic efficiency without significant decrease in activity (Fig. 5d), confirming its high stability and reusability.

Piezocatalytic reduction of uranium mechanism

The mechanism of efficient piezoelectric extraction of UO_2^{2+} was studied. As shown in Supplementary Fig. 18, a new characteristic peak (909 cm^{-1}) attributed to O = U = O is observed in the FT-IR spectrum after piezoelectric catalytic reduction of U(VI), indicating that uranium was attached to the adsorbent[18]. SEM images reveal the presence of numerous spherical crystals and amorphous uranium distributed on the surface of ZnO@COF-40 after ultrasonic treatment (Supplementary Fig. 19). Energy spectrum analysis (EDS) shows that these spherical crystals are primarily composed of uranium and oxygen elements, indicating that uranium oxides are formed after uranium reduction (Supplementary Fig. 20). Subsequently, the valence states of uranium on ZnO@COF-40 after piezoelectric catalysis were studied using XPS. In the survey spectra of ZnO@COF-40 + U (Supplementary Fig. 21), distinct U 4*f* and U 4*d* peaks are observed compared to the sample before adsorption. Further analysis of high-resolution spectra (Supplementary Fig. 22) reveals the coexistence of both U(VI) and U(IV) in different valence states of uranium. The U 4*d* peak is attributed to U_3O_7, proving the presence of both U(IV) and U(V) oxidation states[46]. This demonstrates the transformation of uranium in various valence states during the process of uranium extraction using ZnO@COF-40 piezoelectric catalysis. PXRD experiments were conducted to further analyze the uranium oxide obtained after the reaction. As shown in Supplementary Fig. 23, ZnO@COF-40 exhibits new characteristic peaks at 12.03° and 28.26° after uranium extraction. Upon meticulous examination, these peaks are identified as UO_3•$2H_2O$ (PDF 13-0241) and UO_2 (PDF 36-0089), consistent with the oxidation states determined by XPS analysis. Hence, it is speculated that ZnO@COF-40 may first reduce UO_2^{2+} to UO_2 in the process of piezoelectric catalytic uranium extraction. Subsequently, UO_2 is rapidly oxidized to U_3O_7 when exposes to air, and further oxidizes to UO_3•$2H_2O$. To validate this hypothesis and further elucidate the mechanism of the piezocatalytic catalytic process, various radical scavengers were employed during the extraction process. As shown in Supplementary Fig. 24, the presence of p-BQ and DDQ significantly reduce the removal of U(VI), indicating that $•O_2^-$ and e^- are the main active species in the piezoelectric catalytic process. This phenomenon results from the generation of a significant quantity of h^+ and e^- by ZnO@COF-40 under ultrasonic irradiation (Supplementary Fig. 25). Some electrons on the surface of the material directly promote the reduction of UO_2^{2+} to UO_2, while other electrons reduce soluble oxygen to $•O_2^-$[47]. Subsequently, $•O_2^-$ further contributes to the reduction of UO_2^{2+} to UO_2.

To gain deeper insights into the interface interactions between ZnO and COF after their composite, density functional theory (DFT) calculations were performed. To elucidate the origin of charge transfer across the interface, the work functions (WF) of ZnO and COF were determined by aligning their Fermi level with the vacuum level (Fig. 6a, b). The WF of ZnO is 5.38 eV, while that of COF is 4.87 eV, indicates the higher electrostatic potential of COF than ZnO, leading to the establishment of an interface electric field at the ZnO@COF-40 interface (Fig. 6c). Due to the difference in WF, electrons are driven from COF to ZnO, inevitably resulting in a decrease in electron density on the COF side and an increase in electron density on the ZnO side. This in turn alleviates the shielding effect of ZnO metal edge states. Based on this, the charge transfer mechanism of ZnO@COF-40 catalytic reduction of uranium under ultrasonic treatment was proposed. The construction of Z-type heterojunction in ZnO@COF-40 eliminates the edge shielding effect of ZnO metallic state and promotes efficient electron transfer within the structure. Under mechanical stimulation, ZnO is excited to generate a significant piezoelectric potential, effectively facilitating the separation of free electrons and holes. Simultaneously, the excited electrons on the conduction band (CB) of ZnO are transferred to the valence band (VB) of COF. During the catalytic reduction of uranium, U(VI) in solution is adsorbed on the active site of COF. Under ultrasound treatment, electrons on the CB of COF are transferred to the LUMO orbitals of U(VI), resulting in the reduction of U(VI) to U(IV) (Fig. 6d). In summary, the ZnO@COF-40 heterojunction can effectively extract uranium under simple mechanical stress. This work greatly enhances the understanding of COF's role in improving the piezoelectric properties of two-dimensional materials, providing valuable insights into the design and optimization of piezoelectric catalytic materials.

Uranium extraction under simulated ocean waves

Based on the excellent performance of ZnO@COF-40 in uranium extraction, the research has been carried out on the extraction of uranium from spiked seawater with ZnO@COF-40. As shown in Supplementary Fig. 26, ZnO@COF-40 performs almost as well in seawater as in pure water. In 10 ppm U spiked seawater, the extraction efficiency of U(VI) by ZnO@COF-40 is as high as 98.53% within 1 min under ultrasonic. Encouraged by this, the potential application of ZnO@COF-40 in uranium extraction from natural seawater was further investigated. As shown in Supplementary Fig. 27, the experimental setup simulated a dynamic ocean environment, which generated surface waves with the velocity of about 1.54 cm s^{-1}, slightly lower than the average velocity in the coastal marine area (2-3 cm s^{-1}), but enough to replicate the dynamics of real waves[48]. Within this simulated environment, ZnO@COF exhibits high selectivity and fast uptakes with uranium extraction capacity of 37.8 mg g^{-1} in seawater after 5 days (Supplementary Fig. 28). The average daily uranium extraction capacity is 7.56 mg g^{-1} d^{-1}, meaning that ZnO@COF-40 can achieve the preset target of the UES standard (6 mg g^{-1}) in one day[49]. Additionally, a comprehensive comparison of ZnO@COF-40 with previously reported uranium extraction catalysts and adsorbents shows that its performance is at the top of the list (Supplementary Fig. 29 and Supplementary Table 3). ZnO@COF demonstrates exceptional extraction efficiency and kinetics, which further proves the advantages of piezoelectric catalytic uranium extraction. These results reveal the potential for ZnO@COF to efficiently capture uranium from seawater under simulated low-energy wave conditions and mark the first successful use of wave energy to recover uranium resources, providing an innovative strategy to address the global energy crisis.

Discussion

In summary, we have successfully synthesized a Z-type heterojunction piezoelectric catalyst named ZnO@COF-40, which exhibited remarkably high piezoelectric catalytic activity. The unique core-shell

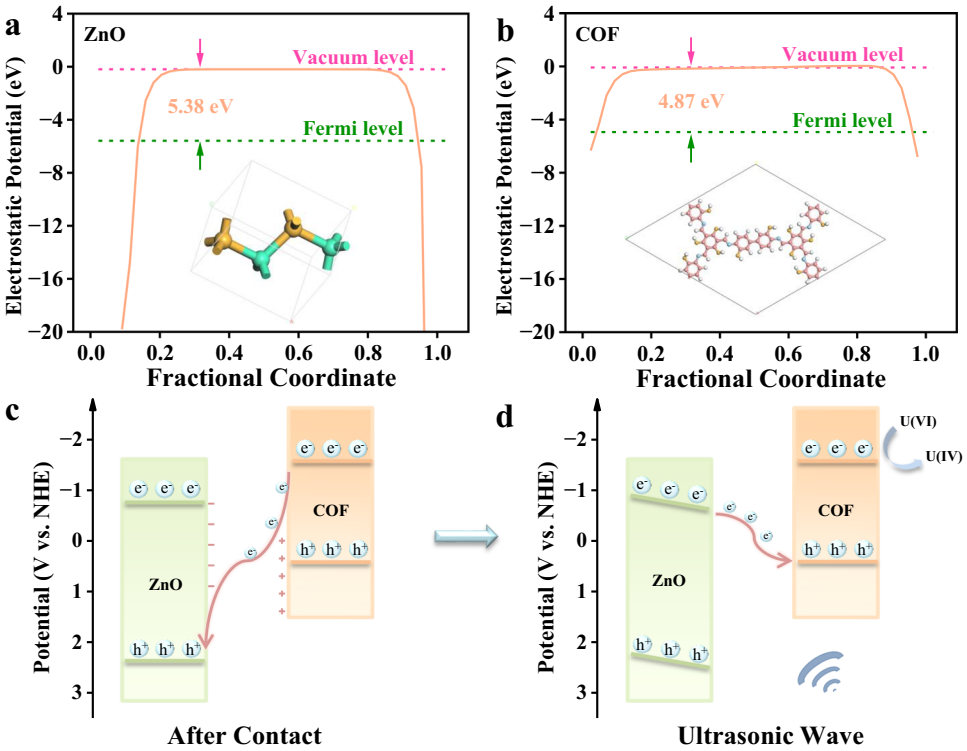

Fig. 6 | Mechanism of ZnO@COF piezoelectric catalysis reduction of uranium. The WF of **a** ZnO (Zn: green; O: orange) and **b** COF (C: pink; N: light blue; O: orange; H: white) calculated by DFT. Schematic representation of **c** charge transfer process and **d** piezocatalytic mechanism of heterojunction. Source data for Fig. 6 are provided as a Source Data file.

encapsulation structure provided a high-speed channel for electron transfer, abundant active sites and higher stability between ZnO and COF. The heterojunction's engineering between ZnO and COF increased the polarity of ZnO, reinforcing piezoelectric polarization. In real seawater experiments, ZnO@COF demonstrated a daily extraction capacity of 7.56 mg g^{-1} d^{-1}, superior to most of the state-of-the-art materials. Consequently, this research marks a significant advance in the regulation of mechanical energy harvesting in piezoelectric materials, introducing a unique and effective strategy for the extraction of heavy metal ions and wastewater treatment.

Methods

Materials and reagents

$Zn(OAc)_2 \cdot 2H_2O$ and diglycol were purchased from Aladdin Co., Ltd. 3-Aminopropyltriethoxysilane (APTES) was obtained from Sarn Chemical Technology Co., Ltd. 2,4,6-trifomylphloroglucinol (TP) and 3,3'-dihydroxybenzidine (BDOH) were obtained from Jilin Chinese Academy of Sciences-Yanshen Technology Co., Ltd. 1,4-dioxane, mesitylene, tetrahydrofuran (THF), acetic acid, and NaOH were purchased from Energy Chemical Co., Ltd.

Synthesis of ZnO nanosheets

$Zn(OAc)_2 \cdot 2H_2O$ (2.74 g, 12.5 mmol), NaOH (0.15 g, 3.8 mmol), and diethylene glycol (125 mL) were mixed in a flame-dried 250 mL Schlenk flask under argon. The resulting mixture was then stirred at 200 rpm and heated to 240 °C for 30 min before being rapidly cooled in an ice bath. Following this, ZnO nanospheres were collected by centrifugation, washed twice with 50 mL of acetone, and vacuum-dried.

Synthesis of ZnO-APTES

ZnO nanospheres powder (500 mg) was ultrasonically dispersed in 50 mL of ethanol for 1 h. Then, gradually introduce a solution containing 300 µL APTES and 10 mL ethanol, stirred vigorously at room temperature for 2 h. The mixture was centrifuged, and then washed three times with ultrapure water and ethanol. Finally, the resulting ZnO-APTES was dried at 60 °C for 12 h.

Preparation of COF and ZnO@COF

2.4,6-trifomylphloroglucinol (21.0 mg, 0.10 mmol), 3,3'-dihydroxybenzidine (32.44 mg, 0.15 mmol), and different weight ratios of ZnO-APTES (0-100, referred to COF proportion) were added to a 25 mL Pyrex tube. Then adding mesitylene, 1,4-dioxane (v/v = 1/1, total 4 mL) and acetic acid (0.5 mL, 6 M), and the mixture was sonicated for 15 min, degassed by three freeze-pump-thaw cycles, sealed under vacuum and heated at 120 °C for 3 days. A yellowish-brown precipitate was collected by filtration, washed with THF, CH_2Cl_2 and methanol, then Soxhlet extracted in CH_2Cl_2 and methanol for 24 h and dried under vacuum at 60 °C for 12 h to obtain COF (TP-BDOH) and ZnO@COF-x (x = 10, 20, 40, and 60). ZnO-APTES and COF were physically mixed in a mass ratio of 3:2 and named as ZnO/COF-40.

Reporting summary

Further information on research design is available in the Nature Portfolio Reporting Summary linked to this article.

Data availability

All the data that support the findings of this study are available within the paper and its Supplementary Information files. Source data are provided with this paper. Additional data are available from the corresponding authors upon request. Source data are provided with this paper.

References

1. Wiechert, A. I., Yiacoumi, S. & Tsouris, C. The ocean's nuclear energy reserve. *Nat. Sustain.* **5**, 13–14 (2022).

2. Tsouris, C. Uranium extraction: Fuel from seawater. *Nat. Energy* **2**, 17022 (2017).
3. Zhang, S. et al. Confining Ti-oxo clusters in covalent organic framework micropores for photocatalytic reduction of the dominant uranium species in seawater. *Chem* **9**, 3172–3184 (2023).
4. Pei, X. et al. Synthesis of quinone-amine-linked covalent organic frameworks for boosting the photocatalytic removal of uranium. *Adv. Funct. Mater.* **24**, 10827 (2024).
5. Li, F.-F. et al. Stable sp^2 carbon-conjugated covalent organic framework for detection and efficient adsorption of uranium from radioactive wastewater. *J. Hazard. Mater.* **392**, 122333 (2020).
6. Cui, W.-R. et al. Regenerable covalent organic frameworks for Photo-enhanced uranium adsorption from seawater. *Angew. Chem. Int. Ed.* **59**, 17684–17690 (2020).
7. Cui, W.-R. et al. Regenerable and stable sp^2 carbon-conjugated covalent organic frameworks for selective detection and extraction of uranium. *Nat. Commun.* **11**, 436 (2020).
8. Yang, H. et al. Tuning local charge distribution in multicomponent covalent organic frameworks for dramatically enhanced photocatalytic uranium extraction. *Angew. Chem. Int. Ed.* **62**, e202303129 (2023).
9. Abney, C. W., Mayes, R. T., Saito, T. & Dai, S. Materials for the recovery of uranium from seawater. *Chem. Rev.* **117**, 13935–14013 (2017).
10. Yuan, Y. et al. Selective extraction of uranium from seawater with biofouling-resistant polymeric peptide. *Nat. Sustain.* **4**, 708–714 (2021).
11. Chen, T. et al. Advanced photocatalysts for uranium extraction: Elaborate design and future perspectives. *Coord. Chem. Rev.* **467**, 214615 (2022).
12. Chen, Z. et al. Tuning excited state electronic structure and charge transport in covalent organic frameworks for enhanced photocatalytic performance. *Nat. Commun.* **14**, 1106 (2023).
13. Zhang, H. et al. Three mechanisms in one material: Uranium capture by a polyoxometalate–organic framework through combined complexation, chemical reduction, and photocatalytic reduction. *Angew. Chem. Int. Ed.* **58**, 16110–16114 (2019).
14. Niu, C.-P., Zhang, C.-R., Liu, X., Liang, R.-P. & Qiu, J.-D. Synthesis of propenone-linked covalent organic frameworks via Claisen-Schmidt reaction for photocatalytic removal of uranium. *Nat. Commun.* **14**, 4420 (2023).
15. Chen, Y. et al. Selective recovery of precious metals through photocatalysis. *Nat. Sustain.* **4**, 618–626 (2021).
16. Yang, H. et al. Functionalized iron–nitrogen–carbon electrocatalyst provides a reversible electron transfer platform for efficient uranium extraction from seawater. *Adv. Mater.* **33**, 2106621 (2021).
17. Liu, C. et al. A half-wave rectified alternating current electrochemical method for uranium extraction from seawater. *Nat. Energy* **2**, 17007 (2017).
18. Zhang, C.-R. et al. A novel 3D sp^2 carbon-linked covalent organic framework as a platform for efficient electro-extraction of uranium. *Sci. China Chem.* **66**, 562–569 (2023).
19. Zhai, H., Ding, S., Chen, X., Wu, Y. & Zhong, L. Z. Advances in solid–solid contacting triboelectric nanogenerator for ocean energy harvesting. *Mater. Today* **65**, 166–188 (2023).
20. Stokstad, E. A reboot for wave energy. *Science* **352**, 637–638 (2016).
21. Liu, W. et al. Directing charge transfer in a chemical-bonded $BaTiO_3$@ReS_2 schottky heterojunction for piezoelectric enhanced photocatalysis. *Adv. Mater.* **34**, 2202508 (2022).
22. Zhou, X., Shen, B., Lyubartsev, A., Zhai, J. & Hedin, N. Semiconducting piezoelectric heterostructures for piezo- and piezo-photocatalysis. *Nano Energy* **96**, 107141 (2022).
23. Shen, P. et al. Ultra-fast piezocatalysts enabled by interfacial interaction of reduced Graphene Oxide/MoS_2 heterostructures. *Adv. Mater.* **35**, 2212172 (2023).
24. Xu, M.-L. et al. Piezo-photocatalytic synergy in $BiFeO_3$@COF Z-Scheme heterostructures for high-efficiency overall water splitting. *Angew. Chem. Int. Ed.* **61**, e202210700 (2022).
25. Hu, C. et al. Orthogonal charge transfer by precise positioning of silver single atoms and clusters on carbon nitride for efficient piezocatalytic pure water splitting. *Angew. Chem. Int. Ed.* **61**, e202212397 (2022).
26. Zhang, J. et al. Piezoelectric enhanced peroxidase-like activity of metal-free sulfur doped graphdiyne nanosheets for efficient water pollutant degradation and bacterial disinfection. *Nano Today* **43**, 101429 (2022).
27. Yu, C. et al. Selective enhancement of photo-piezocatalytic performance in $BaTiO_3$ via heterovalent ion doping. *Adv. Funct. Mater.* **32**, 2209365 (2022).
28. Zhao, S. et al. Harvesting mechanical energy for hydrogen generation by piezoelectric metal–organic frameworks. *Mater. Horiz.* **9**, 1978–1983 (2022).
29. Tian, W. et al. Efficient piezocatalytic removal of BPA and Cr(VI) with SnS_2/CNFs membrane by harvesting vibration energy. *Nano Energy* **86**, 106036 (2021).
30. Yang, X. & Daoud, W. A. Triboelectric and piezoelectric effects in a combined tribo-piezoelectric nanogenerator based on an interfacial ZnO nanostructure. *Adv. Funct. Mater.* **26**, 8194–8201 (2016).
31. Pan, Z., Peng, W., Li, F. & He, Y. Carrier concentration-dependent piezotronic and piezo-phototronic effects in ZnO thin-film transistor. *Nano Energy* **49**, 529–537 (2018).
32. Kim, M. & Fan, J. Piezoelectric properties of three types of PVDF and ZnO nanofibrous composites. *Adv. Fiber Mater.* **3**, 160–171 (2021).
33. Pan, Z., Peng, W., Li, F., Cai, Y. & He, Y. On the piezo-phototronic effect in Si/ZnO heterojunction photodiode: the effect of the fermi-level difference. *Adv. Funct. Mater.* **30**, 2005996 (2020).
34. Keil, P. et al. Piezotronic tuning of potential barriers in ZnO bicrystals. *Adv. Mater.* **30**, 1705573 (2018).
35. Liu, C. et al. Interface engineering on p-CuI/n-ZnO heterojunction for enhancing piezoelectric and piezo-phototronic performance. *Nano Energy* **26**, 417–424 (2016).
36. Wu, Y. et al. Integrated unit-cell-thin MXene and Schottky electric field into piezo-photocatalyst for enhanced photocarrier separation and hydrogen evolution. *Chem. Eng. J.* **439**, 135640 (2022).
37. Ning, X., Hao, A., Chen, R., Khan, M. F. & Jia, D. Constructing of GQDs/ZnO S-scheme heterojunction as efficient piezocatalyst for environmental remediation and understanding the charge transfer mechanism. *Carbon* **218**, 118772 (2024).
38. Son, S. U. et al. Core-shell ZnO@microporous organic polymer nanospheres as enhanced piezo-triboelectric energy harvesting materials. *Angew. Chem. Int. Ed.* **61**, e202209659 (2022).
39. Lan, S. et al. Piezo-modulated interface field facilitating hydroxyl radical formation of $SrTiO_3$/ZnO heterojunction for water purification. *Chem. Eng. J.* **499**, 155862 (2024).
40. Zhang, M. et al. Semiconductor/covalent-organic-framework Z-Scheme heterojunctions for artificial photosynthesis. *Angew. Chem. Int. Ed.* **59**, 6500–6506 (2020).
41. Calik, M. et al. Extraction of photogenerated electrons and holes from a covalent organic framework integrated heterojunction. *J. Am. Chem. Soc.* **136**, 17802–17807 (2014).
42. Bao, S. et al. TpBD COF@$ZnIn_2S_4$ nanosheets: A novel S-scheme heterojunction with enhanced photoreactivity for hydrogen production. *Appl. Catal. B: Environ.* **330**, 122624 (2023).
43. Liu, X. et al. Covalent organic framework modified carbon nanotubes for removal of uranium (VI) from mining wastewater. *Chem. Eng. J.* **450**, 138062 (2022).
44. Zhang, Y. et al. ZnO/COF S-scheme heterojunction for improved photocatalytic H_2O_2 production performance. *Chem. Eng. J.* **444**, 136584 (2022).

45. Yang, X., Lan, X., Zhang, Y., Li, H. & Bai, G. Rational design of MoS_2@COF hybrid composites promoting C-C coupling for photocatalytic CO_2 reduction to ethane. *Appl. Catal. B: Environ.* **325**, 122393 (2023).
46. Leinders, G., Bes, R., Kvashnina, K. O. & Verwerft, M. Local structure in U(IV) and U(V) environments: the Case of U_3O_7. *Inorg. Chem.* **59**, 4576–4587 (2020).
47. Liang, R. et al. Boosting the photoreduction uranium activity for donor–acceptor–acceptor type conjugated microporous polymers by statistical copolymerization. *Sep. Purif. Technol.* **312**, 123291 (2023).
48. Johnson, M. & Niebauer, H. J. The 1992 summer circulation in the Northeast Water Polynya from acoustic Doppler current profiler measurements. *J. Geophys. Res. Oceans.* **100**, 4301–4307 (1995).
49. Mollick, S. et al. Benchmark uranium extraction from seawater using an ionic macroporous metal–organic framework. *Energy Environ. Sci.* **15**, 3462–3469 (2022).

Acknowledgements

J.-D.Q. acknowledges support from the National Natural Science Foundation of China (22036003 and 22376023) and the Natural Science Foundation of Jiangxi Province (20232BBE50031). R.-P.L. acknowledges support from the National Natural Science Foundation of China (22176082).

Author contributions

J.-D.Q., R.-P.L. and J.-X.Q. conceived and designed the research. J.-X.Q. and J.-W.G. performed the synthesis and conducted the experiments. J.-X.Q., J.-W.G., C.-R.Z., Z.-H.P., Y.-J.C., X.L., J.-L.L. and X.-J.C. performed the characterizations. J.-X.Q., R.-P.L. and J.-D.Q. participated in drafting the paper and gave approval to the final version of the manuscript.

Competing interests

The authors declare no competing interests.

Additional information

Supplementary information The online version contains supplementary material available at https://doi.org/10.1038/s41467-025-56471-z.

Correspondence and requests for materials should be addressed to Jian-Ding Qiu.

Peer review information *Nature Communications* thanks the anonymous reviewer(s) for their contribution to the peer review of this work. A peer review file is available.